From mixing to displacement of miscible phases in porous media: The role of heterogeneity and inlet pressures

Yahel Eliyahu-Yakir,* Ludmila Abezgauz, and Yaniv Edery†
Technion –Israel Institute of Technology, Haifa 3200003, Israel
and École Polytechnique Fédérale de Lausanne (EPFL), Civil Engineering Institute, LCH, 1015 Lausanne, Switzerland

(Received 17 December 2023; accepted 10 July 2024; published 2 August 2024)

Miscible multiphase flow in porous media is a key phenomenon in various industrial and natural processes, such as hydrogen storage and geological carbon sequestration. However, the parameters controlling the patterns of displacement and mixing in these flows are not completely resolved. This study delves into the effects of heterogeneity and inlet pressure on mixing and displacement patterns of low-viscosity miscible phase invasion into a high-viscosity resident phase, that is saturating a porous medium. The findings highlight the substantial influence of inlet pressures and heterogeneity levels in transitioning from uniform to fingering patterns at the pore scale. These phenomena are detectable at the Darcy scale, and their transition from a uniform front to finger formation is effectively marked through a modified Sherwood number. This modified Sherwood number links microscale patterns to physical properties such as velocity distribution, diffusion, and viscosity contrasts. Additionally, the study employs breakthrough curve (BTC) analysis to illustrate the role of higher heterogeneity and inlet pressure in broadening the fluid velocity distribution, leading to the fingering pattern. These research insights provide a nondimensional approach that scales the BTCs, and can serve future models of miscible phase flow in porous media, linking pore-scale dynamics with macroscale Darcy-scale observations.

DOI: 10.1103/PhysRevFluids.9.084501

I. INTRODUCTION

Miscible multiphase flow in porous media is a process where a resident phase is displaced by a different phase within the confinement of a porous structure, and while the phases are different in their characteristics (e.g., density, viscosity, etc.), they can still mix and form an intermediate phase that has characteristics different from both phases. This process is omnipresent in many processes, such as water remediation, hydrogen storage in the subsurface, moisture, and solute transport in soils and geological carbon sequestration [1–5]. In these processes and others, a less viscous phase displaces a resident phase, resulting in increased mobility and causing a fingering pattern due to phase interface instability known as "viscous fingering" [6]. Specifically for hydrogen storage and CGS in brine aquifers, the mixing then leads to the acidification of the brine and potential alterations in rock formations and porosity [5,7–14].

The main bulk of miscible multiphase flow research was done on two-dimensional (2D) Hele-Shaw (HS) cells, where a resident phase residing between two circular plates is displaced by the less viscous miscible phase introduced in the plate center [15–18]. As the invasion proceeds,

*Contact author: yahel.eliyahu-yakir@epfl.ch
†Contact author: yanivedery@technion.ac.il

 ©2024 American Physical Society

the interface between the phases is ever growing, due to the circular nature of the invasion, thus reducing the invading phase fluid velocity in the interface. This invasion pattern leads to the said "viscous fingering," where instabilities in the form of small inhomogeneity on the plate lead to a variation of velocity on the phases interface, which is acerbated by the phases viscosity difference [19–22]. Furthermore, research has demonstrated that adjusting the distance between the HS cell plates (commonly referred to as a gap) can regulate instability, and not every gap has the potential to enhance viscous fingering dynamics. As the gap increases, the instability gets suppressed [23], which is aligned with the Homesy correction on the contribution of the gap of the HS cell to the cell permeability [15]. Moreover, studies on miscible phase flow in porous media indicate that the formation of fingering patterns is also influenced by the flow rate [24–26] and the permeability heterogeneity [27]. Therefore, while HS cells highlight the role of viscosity difference among the phases, which is the dominant feature at the volume scale, the porous material highlights the pore structure on the micron scale. Studies on immiscible phase flow at the pore scale showed the dominance of the heterogeneous structure and how it impacts the uneven advancement of the invading phase due to capillary or viscous forces [14,28–32]. While immiscible phases do not mix and lack the resulting viscosity range associated with miscible phase mixtures, they do underscore the relevance of pore scale heterogeneity on the fingering pattern during invasion for high capillary numbers. Moreover, studies performed on miscible phases that do mix showed that the fingers establish the interface between the phases where mixing occurs [33,34]. As such, rigorous experimental investigations exploring the effect of porous media heterogeneity, fluid flow rate, and miscible phases viscosity on fingering pattern and mixing at the pore scale are currently missing and are crucial for accurate modeling efforts [35–38].

This research aims to investigate how the heterogeneity of porous media influences mixing and invasion patterns under different inlet pressures and heterogeneity levels, and bridge the gap between the pore scale and the Darcy scale for miscible phase flow in porous media. Using a 2D porous media model, we examine how low-viscosity fluids interact with high-viscosity fluids at the pore scale, under varying heterogeneity and inlet pressures while monitoring the flow rates. Our findings reveal that both inlet pressures and heterogeneity levels significantly impact fingering patterns, resulting in distinct displacement and mixing behaviors. These pore-scale phenomena are reflected at the Darcy scale through flux measurements, demonstrating that they have broader implications for miscible phase flow in porous media.

II. METHODS AND MATERIALS

To distinguish between the displacement and mixing within the porous media, we fabricated a 2D porous media with dimensions of 4.5 mm in length, 1.3 mm in width, and 0.05 mmp in depth, made out of p olydimethylsiloxane (PDMS), using a microfluidic mold. We patterned the microfluidic mold with four different heterogeneity levels, where the homogenous pattern is a uniform grid of pillars of 50 μm radii, forming an average pore size (R) of 50. These pillars are placed on grid points (x,y) of a square lattice, allowing for some disorder with normalized standard deviations (σ/R) of 0.01, 0.1, and 0.5, forming the heterogeneity levels depicted in Fig. 1(a). To form the disordered pattern, the deviation of each pillar from the grid center was randomly drawn from a normal distribution with the above standard deviation for both x and y.

We performed a fluid-fluid displacement experiment where the invading fluid is double distilled water (DDW) mixed with rhodamine 6G, and the defending resident fluid is glycerol, and both are inert to the material of the cell. The experimental setup is designed to form a sharp interface between the DDW and the glycerol, with no prior mixing, so as to clearly separate the displacement and the mixing of the fluids. The rhodamine 6G dye, which is used as an indicator, is excited by a 488 nm laser and emits at 550 nm wavelength. Therefore, as the glycerol is mixed with DDW, the dye is diluted, and the emission amplitude diminishes. The DDW and glycerol differ in their density ($\rho_{\mathrm{DDW}} = 1$ and $\rho_{\mathrm{gl}} = 1.26$ g/cm^3, respectively) and in their viscosity ($\mu_{\mathrm{DDW}} = 1 \times 10^{-3}$ and $\mu_{\mathrm{gl}} = 1.43$ Pa s, respectively). For each heterogeneity level, we applied three different inlet

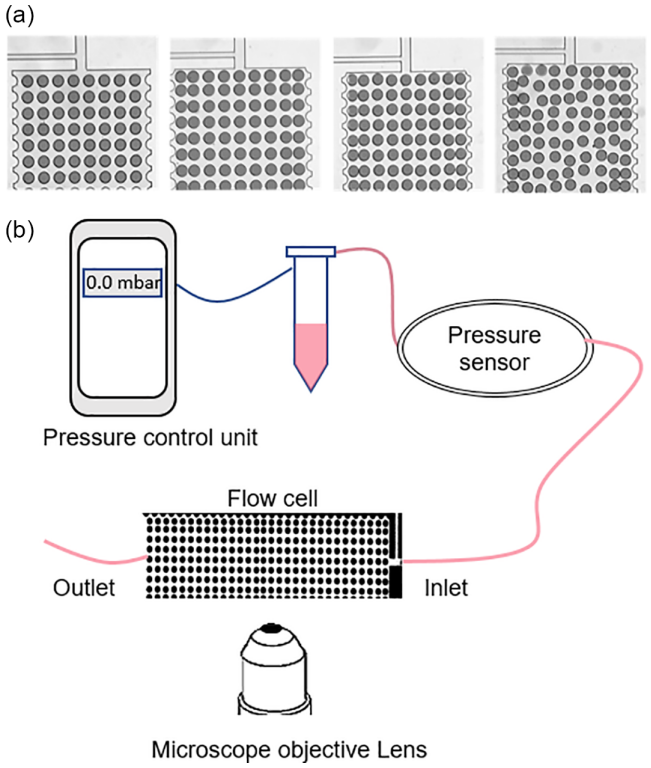

FIG. 1. (a) The 2D flow cells' layout with an obstacle diameter of 50 μm. These obstacles are placed on grid points (x, y) of a square lattice, allowing for some disorder with a normalized standard deviation (σ/R) of 0, 0.01, 0.1, and 0.5 from left to right. (b) The flow cell is connected to a pressure pump controlled by external control units in order to inject the DDW with the rhodamine. The pressure is also continuously monitored at the inlet. The inlet flow is measured with a thermal-based flow sensor that was calibrated for each pressure difference, while the entire fluid-fluid displacement is observed and documented through a confocal microscope.

pressures (15, 30, and 45 mbar, measured at the inlet), while measuring the inlet discharge for every pressure-heterogeneity configuration. In parallel, we developed a MATLAB code to track the invasion of the DDW by the rhodamine fluorescence and the mixing between phases by the fluorescence decrease due to dye dilution, following a verified linear calibration curve matching the fluorescence amplitude to the phases mixing at each pixel [39]. The mixing rate was determined by analyzing the relative intensity within the measured range for each experiment. This range was established per pixel in the flow cell using the initial and final images. Pixels exhibited varying degrees of mixing, reflected in their intensity values. These values were then normalized against the range, yielding a scale from 0 (no mixing) to 1 (complete displacement of the resident fluid by the dyed DDW), indicating the extent of mixing. Using the initial undisplaced and completely displaced images, we directly estimate the thermal white noise error coming from the imaging at less than 1%.

Our experimental configuration entailed monitoring the mixing process using a confocal microscope (Nikon Eclipse Ti2-FP) and a camera (Prime Sigma BSI express) with a frame rate of 0.3 s per frame. The flow cell was connected to a pressure pump (Fluigent; with a pressure range of 345 and 69 mbar) to maintain precise and constant pressure while recording the inlet pressure and the discharge changes over time (Fluigent pressure and discharge sensor M\S, respectively). The reported error by Fluigent for the discharge is 5%, which is in line with the measurement noise we get. This monitoring took place through a 1-mm-thick borosilicate glass slide (Thermo,

Menzel-Glaser), uniformly coated with PDMS using a spin-coating process, and bounded to the flow cell.

III. RESULTS AND DISCUSSION

The experimental setup, described in the Methods and Materials section, allows us to track the invasion of the DDW through the resident glycerol and account for the mixing of the phases and the invasion pattern. We will examine the influence of different heterogeneity levels and inlet pressure on three different spatial and temporal aspects: the invading pattern, the mixing pattern, and the overall flux change.

A. Heterogeneity and the invasion pattern

Pore-scale heterogeneity of porous media is the outcome of pore size variation that dictates the ratio of surface frictional forces on the flowing fluid, while the fluid viscosity determines the magnitude of these frictional forces. Through these frictional forces, the heterogeneity in the flow cell causes variation in the local velocity due to the connectivity among pores and their sizes along the cell thus forming a preferable path with less overall resistance. The velocity profile within each pore is affected by the shear stress that originates from the pore boundaries due to the non;slip condition; meaning, that the velocity decreases with the pore cross section, leading to higher resistance. This pore-size resistance mechanism scales with the fluid's viscosity due to its relationship to the shear stress [40,41]. Therefore, in a porous media experimental setup, a change in the resistivity is expected compared to the HS cells, yet the coupling between the heterogeneity, resistivity change, and invasion pattern is currently missing. We observe that in the homogenous porous medium, the point source inlet for the DDW dictates an initial invasion plume that, over time, evolves into a uniform invasion front despite the point source origin (see Fig. 6, with $\sigma/R = 0.0$ and pressure of 30 mbar in the Appendix). This uniform front is different from the mechanism of viscous fingering in HS cells where one would expect a single finger to emerge [26]. Keeping the same fluids and pressure head while increasing the heterogeneity level, as stated in the Methods and Materials section, leads to a change in the invasion pattern of the DDW in the resident glycerol. The uniform front in the homogeneous configuration switches to a single finger that becomes thinner and more pronounced as the heterogeneity increases, captured by the invasion pattern morphology differences between $\sigma/R = 0.01$ to 0.1, and especially 0.5 (see Fig. 6 in the Appendix). These morphological changes in the invasion pattern suggest that the initial fingering, due to the large viscosity difference, is secondary to the porous media heterogeneity. Specifically, in our experiment, the less viscous fluid reduces the resistance and increases the velocity at each pore it invades, whether by replacing the resident phase or by mixing with it. Therefore, the fingering pattern is the result of both (1) a pore-size resistance mechanism and (2) viscosity evolution at the pore scale. These two processes are coupled; initially, the fingering pattern follows the inner structure and then develops due to the viscous differences among the pores. In contrast, the symmetrical inner structure of the homogenous porous media leads to an even pore-size resistance mechanism, and although there are viscosity differences, due to the fluid distribution within the pore structure, the uniform pore pressure suppresses the fingering pattern. Hence, the spatially uniform pore-size resistance mechanism damps the viscous fingering pattern for the homogeneous case, even though the less viscous fluid invades through a point source at the cell center, which should encourage the emergence of a single finger. As such, in the homogeneous case, the invading phase forms a uniform front due to the uniform pore sizes, which homogenizes the applied frictional forces on the fluid, and, as a result, the pore pressure over the cross section. As the heterogeneity increases, the pore-size variations lead to nonuniform frictional forces and nonuniform pore pressure, leading to velocity variation [42]. This nonuniform invasion pattern leads to spatial variations in viscosity, which further enhances the nonuniform invasion pattern, thus the heterogeneity rate determines the

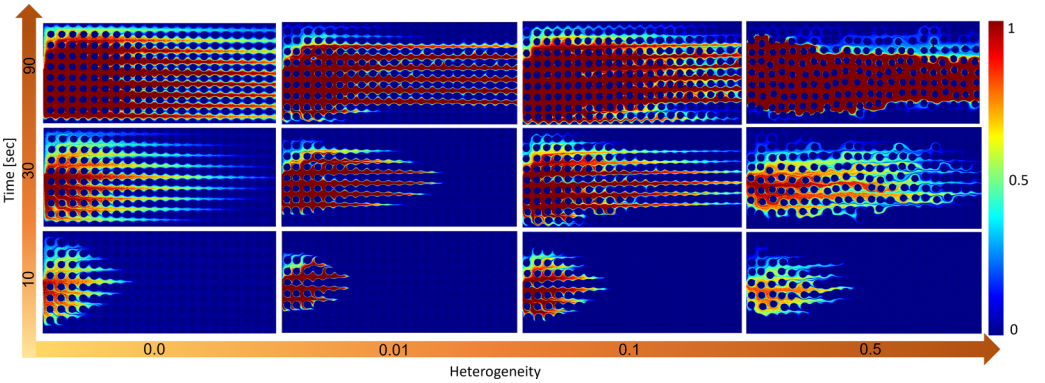

FIG. 2. An image analysis depicting the local mixing and displacement for flow cells with heterogeneity levels of 0.0, 0.01, and 0.5 for an applied inlet pressure of 30 mbar at three different times: 10, 30, and 90 s. Note that blue denotes 100% glycerol and 0% DDW, while red represents 100% DDW and 0% glycerol.

invading pattern, while the viscosity change enhances the invasion pattern. This further exemplifies the strong impact of the inner structure on the flow pattern.

B. Heterogeneity and the interplay between mixing and displacement

As stated earlier, the observed invasion pattern varies from uniform at the homogeneous case to finger formation as the heterogeneity level increases, yet this observation is focused on the displacement of the fluids, while the effect of pore structure on the fluids mixing is missing. Using a calibration curve in Fig. 6, the mixing and displacement pattern among the fluids, due to heterogeneity levels, can be observed in Fig. 2. In the homogeneous cell ($\sigma/R = 0.0$), the uniform fluid invasion forms a uniform mixing front with the resident fluid, followed by the displacing fluid. The mixing front maintains the same initial width, with a maximal mixing level in the middle of the front, a remnant to the point source boundary condition. However, as the heterogeneity rate increases ($\sigma/R = 0.01$, 0.1, and 0.5), the mixing front is less uniform, and a "fingerlike" pattern emerges. The displacing front still follows the mixing front, yet at a smaller cross section within the flow cell; thus, glycerol remains trapped from both sides of the formed finger. Focusing on the maximum heterogeneity level of $\sigma/R = 0.5$, there is a connected finger from the inlet to the outlet within 90 s, while mixing occurs towards the edges of the cell as the finger thickens. As such, the heterogeneity level affects not only the invading pattern but also the mixing pattern, as the main bulk of mixing occurs after the fast finger formation, followed by the finger thickening, in contrast to the homogeneous case, where the bulk of mixing occurs in the front of the invasion. This fingerlike invasion pattern combines different mechanisms that yield dynamic resistance. Initially, the flow follows the pore structure through a preferable path with the lowest resistance. Over time, this path remains preferable not only due to the pore structure but also due to the reduced viscosity, and the mixing is reduced to the edges of the finger. Yet this mixing with the trapped glycerol on the sides must increase the overall fluid viscosity.

C. Discharge change in time as an indicator of spatial displacement and mixing pattern

The pore-scale heterogeneity that causes variation in resistance within the flow cell, leads to changes in viscosity over time and space that must affect the duration required for the invading fluid to reach complete saturation. This change in the displacement time is indicative of the invading phase discharge, as it is basically a change of the invading phase volume occupancy in time within the flow cell. Specifically, the discharge (Q) must increase in time since the fluid viscosity is reduced by both the displacement and the mixing, thus reducing the cell resistance to flow. However, as

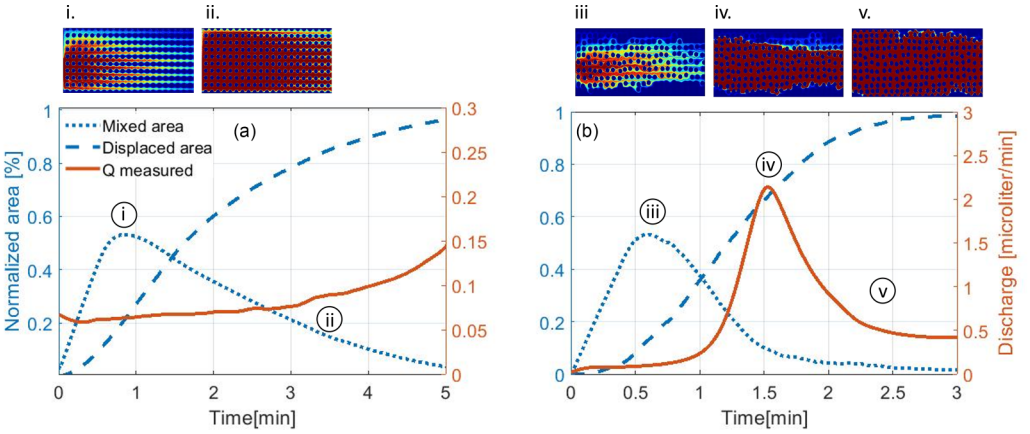

FIG. 3. (a) Homogeneous flow cell. (b) Heterogeneous flow cell ($\sigma/R = 0.0$ and 0.5, respectively), both with an inlet pressure of 30 mbar. The dotted blue line represents the normalized area occupied by a mixture of DDW and glycerol, while the dashed blue line represents the normalized area occupied solely by a minimum of 95% DDW, which is the displacing fluid. Discharge with respect to time is marked by the solid orange line, while (a-i). and (a-ii) mark the maximum mixed volume and displaced volume in the cell, respectively, and (b-iii), (b-iv), and (b-v) mark the maximum mixed volume, the discharge signature for the finger formation, and displaced volume in the cell, respectively.

the invasion pattern changes with the different heterogeneity and inlet pressures, as indicated in the previous Sec. III B, so will the discharge increase rate. To understand the coupling between heterogeneity and discharge, we first focus on the discharge change over time for the extreme cases of completely homogeneous and very heterogeneous porous structures, marked by the orange line in Figs. 3(a) and 3(b), respectively. These changes in discharge over time are coupled with the mixing and displacement volume normalized by the flow cell volume, marked by the dotted and dashed blue lines, respectively, in Figs. 3(a) and 3(b). For the homogeneous case in Fig. 3(a), the discharge slope is constant until 200 s, due to the high glycerol content in the front of the cell that moderates the resistance change. However, DDW mixing in the interface constantly reduces the overall fluid viscosity and therefore, flow cell resistance. Furthermore, the displaced fluid behind the mixed area further decreases the resistance to the flow, which leads to a constant increase in the discharge. When the DDW front reaches the end of the cell, most of the cell is saturated with DDW [point (ii) in Fig. 3(a)], which causes the resistance of the cell to decrease dramatically, and as a result, to a rapid increase in the discharge. In contrast, for the heterogeneous cell in Fig. 3(b), the invading phase flows in a preferable path, or "finger." When the finger reaches the end of the cell, the discharge is at its maximum, as the resistance within the preferable path is at its lowest due to the viscosity drop, and due to the small cross section of the finger with a limited surface area of the solid that further reduces the shear force. After the finger formation, the discharge drops due to mixing towards the edges of the cell, from point iv to point v in Fig. 3(b), and this mixing phase leads to the saturation of the entire cell. As such, the peak in $Q(t)$ indicates a finger pattern in time, which has an initial displacement followed by a mixing phase. Therefore, the external discharge measurement provides a signature to the displacement and mixing mechanisms presented in the previous section. Moreover, it is clear that the same mechanism that leads to the change in local velocity, due to the pore structure heterogeneity and viscosity change in time, also affects the flux measurements, which is the spatial integration of local velocities over the cross-sectional area. However, this measurement differs in the fact that it is made over the whole flow cell on the macroscale and can be considered a Darcy measurement. Therefore, the pore-scale mechanism that leads to the change in invasion pattern has a clear signature at the Darcy scale, which can be measured externally, and is clearly linked to the velocity distribution at the pore scale. The discharge flux measurements of the cell

are distinctively tied to the heterogeneity rate. The discharge measurement averages the local pore fluxes into a single value, representing the total average discharge in the flow cell. Nonetheless, the discharge-time plots vary significantly for different heterogeneity rates, reflecting how pore-level processes affect the overall medium [43,44].

D. Transitioning from front to finger invasion

As shown in the previous section, the level of heterogeneity plays a significant role in shaping the way fluids displace and mix within a cell, primarily by influencing the velocity field. Alongside heterogeneity, inlet pressure also exerts an impact on the scaling of the velocity field. Specifically, the applied inlet pressure serves as an indicator of the spatial distribution of velocity and can be externally scaled by modifying the inlet pressure value. To further investigate the influence of inlet pressure, we conducted identical experiments across all heterogeneity configurations, using three distinct inlet pressure values: 15, 30, and 45 mbar. These results are presented in Fig. 5 as a phase diagram, illustrating how each of these variables (pressure and heterogeneity level) contributes within a matrix configuration, facilitating an examination of their respective influences. As was shown previously, the displacement within the $\sigma/R = 0.5$ flow cell is faster to reach full saturation compared to $\sigma/R = 0.0$, for an inlet pressure of 30 mbar. This relative saturation time is still the case for the inlet pressures of 15 and 45 mbar, and the displacement of the homogeneous $\sigma/R = 0.0$ and the nearly homogeneous case of $\sigma/R = 0.01$ flow cells takes the longest time to be fully saturated by the DDW, while maintaining a uniform displacement with no fingering, as reflected through the discharge rate $[Q(t)]$ measurement pattern. Furthermore, the single-finger formation, with its unique "peak" pattern in the $Q(t)$ measurements, also exists for $\sigma/R = 0.1$, in addition to $\sigma/R = 0.5$ where the heterogeneity level dominates. As the inlet pressure increases, the displacement rate increases, and the peak in the discharge rate appears earlier for the heterogeneous case, forming the connected path between the inlet and outlet faster. Yet as the inlet pressure increases, the fingering pattern also forms for $\sigma/R = 0.01$, where the pore structure configuration is very nearly homogeneous (recall Fig. 1). Apparently, the increase in inlet pressure broadens the narrow velocity distribution by favoring the local viscosity variations, leading to variations in shear forces. The broadening of the velocity distribution leads to relatively high local velocities, which leads to a local reduction in viscosity. This local viscosity reduction shifts the invasion towards a fingering pattern, even though the permeability along the cross section is almost uniform. In a way, higher pressure increases the shear forces and acerbates the small differences in the pore structure, which broadens the velocity distribution; thus transitioning the nearly uniform flow pattern towards a finger formation. In contrast, lower pressures decrease the shear forces, which narrows the velocity distribution. For $\sigma/R = 0.0$, there is no evidence for the fingering pattern even at a high inlet pressure, as there are no spatial velocity variations, due to the highly uniform pore structure; nonetheless, this fingering may still occur for the limiting case of $\sigma/R = 0.0$ through a local instability in the invasion, in which the local viscosity difference will worsen. We expect that as the domain size increases, the chances for this instability that will lead to finger formation will also increase. Fingering patterns have already been observed in simulations of miscible fluid-fluid displacement at homogeneous porous media [37]. However, in our experiments at $\sigma/R = 0.0$, we did not observe this finger pattern for this specific cell length. It is important to note that these simulations were performed in 2D geometry, and initial results from COMSOL 2D simulations done in our laboratory for the homogeneous case, while including the third dimension by the surface area of HS plates as done in [15], show that in two dimensions the displacement pattern is controlled by a single finger. However, performing the same simulation in a full 3D configuration recovered a similar uniform displacement pattern observed in our experiments, marking the importance of experimental observations in this field. We believe that the correction for the added surface area between the 2D and the 3D case is not sensitive enough for miscible phase flow, where the shear forces scale with both pressure and heterogeneity. The observed mixing at the front of the invading phase, together with the specific viscosity ratio of the invading and residence fluids, seem to restrain the fingering pattern. These results are currently out

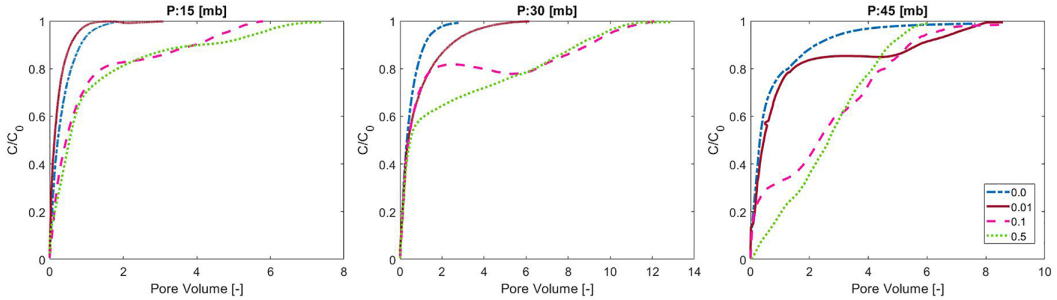

FIG. 4. Breakthrough curves for an inlet pressure of 15, 30, and 45 mbar from left to right.

of the scope of this study and will be presented in a future study comparing the COMSOL simulation with the experiment while accounting for the local shear forces. The fingering pattern may also appear if the cell is made longer (and not necessarily bigger), which will allow the instability that generates the fingers to overcome the suppressing nature of the uniform shear forces applied in the homogeneous case.

E. The finger formation effect on the breakthrough curve tailing

As stated in the previous section, the heterogeneity level and the driving pressure lead to the velocity spatial distribution through the shear stress, which in turn leads to the mixing and displacement pattern of the invading miscible phase. However, in our experiments, we cannot directly measure the velocity distribution, yet we do measure the discharge as an indicator for the displacement pattern, which is an accessible Darcy measurement done indirectly in the laboratory and in the field. Yet there is an additional measurement done in the laboratory and field scale that allows us to analyze concentration changes of the fluid, originating in the pore scale and propagating to the Darcy scale, namely, the breakthrough curve (BTC). The BTC is measured at a scale of pore volume (PV), which is the cumulative inlet volume divided by the cell's volume, and is a dimensionless number that scales the time by the time it takes a single volume to be replaced. Previous studies have related the velocity distribution with the tailing of the BTC [45–47]. These studies indicate that as the velocity distribution at the pore and Darcy scale increases, so does the amount of PV required to replace the resident fluid, forming an increase in the BTC forward tailing. This extended PV required for the replacement is due to the inclusion of the high-viscosity phase that is removed through the mixing mechanism described in Sec. III C. This heavy forward tailing in the BTC is commonly referred to as anomalous transport [44,48,49]. Currently, we will only focus on the BTC tailing as an indicator of the broadening of the velocity distribution, while the nature of the anomalous flow will be the subject of a future study. In the BTC plot, the normalized concentration of the dye, C/C_0, is presented versus the number of PV. This will be done through the measured volume change using the dye concentration image analysis, where C is the volume of the injected fluid and C_0 is the total cell volume. Using the PV to scale the time by the volume exchange time allows us to compare the effect of the dispersion alone as we divide it by the average velocity. As such, the BTC's tailing should be indicative of the velocity field, which is the outcome of the fluid's displacement and mixing patterns.

In Fig. 4, three different inlet pressures are presented: 15, 30, and 45 mbar, and with each increase of the pressure, the differences between the BTCs of various heterogeneity levels become more pronounced. At an inlet pressure of 30 mbar in Fig. 4(a), the system can be divided into two groups: (1) the homogeneous group of $\sigma/R = 0.0$ and 0.01 and (2) the heterogeneous group of $\sigma/R = 0.1$ and 0.5, which follow the fingering pattern. It is possible to distinguish the BTC curve within the heterogeneous group (2) into two curve slopes: steep and moderate. The steep slope represents a low PV time needed to establish the finger from the beginning until it is fully developed to the

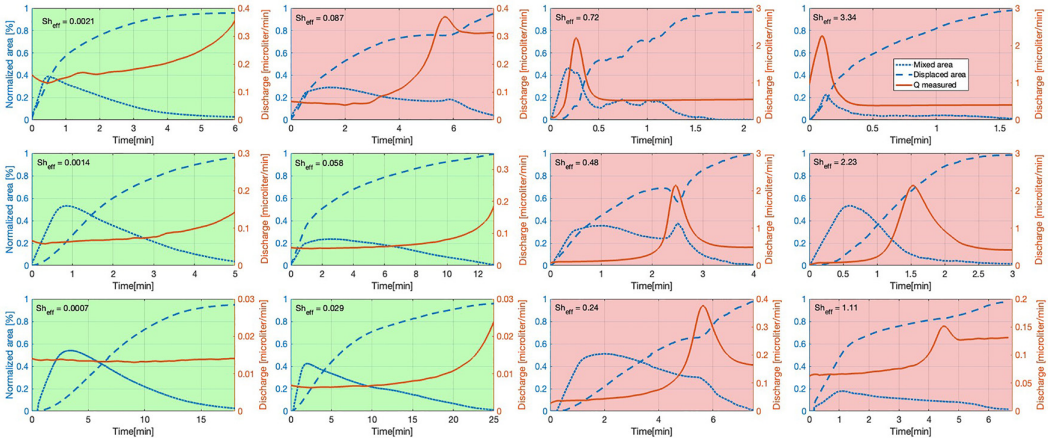

FIG. 5. Phase diagram illustrates how heterogeneity and inlet pressure simultaneously influence the displacement (dashed blue line), the mixing (dotted blue line), and the discharge rate pattern (solid orange line). The green shade marks uniform front invasion identified by the monotonic rise of the flux, and indicated by the $\mathrm{Sh}_{\mathrm{eff}} < 0.06$, while the red shade marks finger invasion identified by the nonmonotonic rise of the flux, and indicated by $\mathrm{Sh}_{\mathrm{eff}} > 0.06$.

inlet-outlet connection with high velocity. Once the finger is steady, the mixing slowly reduces the resident phase volume as the viscosity increases and lowers the velocity, thus requiring more PV; this is the moderate slope, also known as "heavy tail" for a replacement boundary condition (as opposed to a pulse at the inlet that will form a different BTC heavy tail). The moderate slope represents the high amount of PV that was needed to mix and then replace the remaining glycerol from the edges of the cell. Figure 4 shows that the configuration of $\sigma/R = 0.5$ requires the most PV to reach saturation, yet in Fig. 5 the configuration of $\sigma/R = 0.5$ requires the shortest time to reach saturation, and therefore, we understand that the velocity within the formed finger is the highest. This high velocity leads to a larger velocity polarization, and so, the velocity distribution increases. This broadening of the velocity distribution becomes even more significant as the inlet pressure increases, as shown at 45 mbar [Fig. 4(c)]. At this pressure, each heterogeneity level has its own slope, portraying how the increase in the inlet pressure broadens the velocity distribution that affects the pattern of the invading phase, even if the heterogeneity level is only slightly different from the homogeneous configuration. This observation has already been discussed in the context of discharge rate measurement in Fig. 5, supporting the same findings discussed here. Alternatively, as the inlet pressure decreases to 15 mbar, the velocity distribution becomes narrower, resulting in lower differences between heterogeneity levels, as shown in Fig. 4(a).

F. Using the Sherwood number to differentiate the phase diagram

Previous sections analyzed how the transition between the uniform front and the finger formation, set by the change in pressure and heterogeneity configurations, leads to a change in the invasion and mixing pattern (see Fig. 5). This pattern change is also apparent in the BTC measurements, which points to the dominant role of velocity distribution, which is the outcome of shear stresses induced by the pore structure and pressure difference. However, another outcome of this velocity distribution, leading to the pattern change, is the change in the convective mass transfer rate for the invasion pattern relative to the diffusion rate for the mixing, which are the hallmarks of the Sherwood number. The Sherwood number is suitable in our experimental context, as the mixing among the phases must follow the diffusion of both the water phase through the glycerol and the glycerol through the water over their mutual interfaces, while the water advancement scales the rate of convective mass transfer. Following this analogy, we define the convective mass transfer by the

TABLE I. The table depicts the porosity, calculated and measured permeability, and tortuosity for each heterogeneity.

Parameters	σ/R (−)	0.0	0.01	0.1	0.5
	ϕ (−)	0.68	0.64	0.64	0.62
	$k_{KC} \times 10^{-12}$ (M^2)	69.8	40.3	33.9	13.3
	$k_{expt.} \times 10^{-12}$ (M^2)	44	10.02	8.38	8.04
	T (−)	1	1.01	1.1	1.5

glycerol displacement (q) in our system using the Darcy relation:

$$q = -\frac{k}{\mu_{gl} L}\Delta P, \tag{1}$$

where k is the permeability, L is the length of the cell, and we use the dominant viscosity in our setup, namely, μ_{gl}, as it is three orders larger than μ_{DDW}. The permeability can be calculated directly by the Kozeny-Carmen equation:

$$k_{KC} = \frac{\phi^3}{cT^2A^2(1-\phi)^2}, \tag{2}$$

where ϕ is the porosity, c is the spherical coefficient (here equal to 1 as the pillars are round), T is the tortuosity, and A is the hydraulic radii defined as the surface, S, to volume, V ($A = \frac{S}{V}$). The tortuosity can be directly calculated from the normalized standard deviation σ/R, which marks the range for the pillar center movement from a uniform grid using the relation $T = 1 + \sigma/R$. However, we found that there is a discrepancy between the calculated permeability depicted in (2), and the permeability directly measured in the flow cell ($k_{expt.}$). To measure the permeability, various pressure differences were applied while measuring the flux of DDW alone and accounting for pressure loss within the tubes using the Darcy-Weisbach equation (see Table I for details).

As the interface between the phases changes due to the torturous path, we define an effective diffusion coefficient $D_{eff} = \frac{D}{T}$, which scales the diffusion of water into glycerol ($D = 950\ \mu m^2/s$ [50]) with the tortuosity, as shown in many studies [51–54]. This derivation provides the Sherwood number calculated from the permeability and marked by the updated permeability and tortuosity:

$$\mathrm{Sh} = \frac{q}{D_{eff}/R} = \frac{RT k_{expt.}\Delta P}{\mu_{gl} L D}, \tag{3}$$

where R is the mean pore size. As stated earlier, the low-viscosity fluid invades through the low-resistance pore, which further reduces the overall resistance by the viscosity change, leading to higher velocity. Therefore, this equation considers the geometry of the flow cell, yet it does not consider the change in the velocity distribution due to the change in viscosity as the invasion occurs. For that, we approximate the velocity distribution variance by the pore structure variance, as the latter leads to the shear forces that scale the velocity distribution. We then add to the Sherwood number (3) the impact of the high-velocity values due to the DDW phase low viscosity, as marked by one normalized standard deviation, and multiplied with the viscosity contrast ($\mu_C = \frac{\mu_{gl} - \mu_{DDW}}{\mu_{gl} + \mu_{DDW}}$, shown in [25]):

$$\mathrm{Sh}_{eff} = \frac{Rq}{D_{eff}} + \frac{q_{DDW}\sigma/R}{D/w\phi}\mu_C = \frac{k_{expt.}\Delta P}{\mu_{gl} L D}\left(RT + \frac{w\phi\mu_{gl}\sigma}{R\mu_{DDW}}\mu_C\right),$$

where w is the width of the cell, marking the cross-sectional area where the velocity changes due to the DDW invasion marked by the q_{DDW}. This calculated modified Sherwood number has a marked transition around $\mathrm{Sh}_{eff} = 0.06$, as depicted in Table II and in Fig. 5, and above this value the invasion pattern follows a finger formation, while below this value the invasion pattern follows a uniform front (highlighted by a red and green background, respectively, in Fig. 5). Moreover, the

TABLE II. The table depicts the Sherwood and modified Sherwood, by calculating the flux from Eq. (1) using the measured permeability, and applied pressure, for the Sherwood number following (3); and adding to the Sherwood number a single normalized standard deviation for the flux as shown in Eq. (4). The table shows a marked transition around $\mathrm{Sh}_{\mathrm{eff}} = 0.06$, where above it there is a finger formation, and below it, there is a uniform front, in line with Fig. 5.

		$\mathrm{Sh}_{\mathrm{eff}}$				$\mathrm{Sh} \times 10^{-3}$			
P (mbar)	σ/R	0.0	0.01	0.1	0.5	0.0	0.01	0.1	0.5
	45	0.0021	0.087	0.72	3.34	1.6	0.37	0.34	0.45
	30	0.0014	0.058	0.48	2.23	1.1	0.25	0.27	0.29
	15	0.0007	0.029	0.24	1.11	0.5	0.12	0.11	0.15

Sherwood number calculated by (3), scales very differently with the heterogeneity than the modified Sherwood number calculated by (4), while following a similar trend with the applied pressure, stressing the nontrivial role of the heterogeneity in modifying the velocity field distribution, marked by the standard deviation (see Table II for details).

Furthermore, the Sherwood number marks the ratio between the diffusive mixing and the convective mass transfer. As such, the Sherwood number should scale the BTCs for various inlet pressures that alter the flux. To test this scaling, we first replot the BTCs with respect to the inlet pressure for each heterogeneity level (see Fig. 7, column A in the Appendix). As can be seen, although we normalize these BTCs to a PV, they do not overlap on each other even for the homogeneous case. However, when we multiply the PV of these BTCs with the modified Sherwood number (Fig. 7, column B in the Appendix), the homogeneous BTCs overlap very well. As the heterogeneity increases, their overlapping features still hold for the initial rise of the BTCs, but not the features after the finger formation. This scaling indicates that the mixing and convective timescales, which are the result of the inlet pressure, are also important and allow us to interpret the results through the modified Sherwood number. Thus, using only known and measurable quantities in the experimental setup while approximating the broadening of the velocity distribution by the added normalized standard deviation, the observed pattern transition between the finger to the uniform front is captured through the modified Sherwood number in a phenomenological way.

IV. SUMMARY AND DISCUSSION

This experimental investigation explores the impact of heterogeneity and inlet pressure on mixing patterns in porous media, using a 2D model to study interactions between low- and high-viscosity fluids. The research reveals that both inlet pressures and heterogeneity levels crucially influence fingering patterns, leading to variations in fluid displacement and mixing behaviors at the pore scale. These phenomena are observable at the Darcy scale through flux measurements featuring the transition between uniform and finger formation. This transition can be captured by a modified Sherwood number that phenomenologically links these microscale patterns to physical properties such as velocity distribution, mixing through diffusion, and viscosity contrasts. This transition is also apparent in the BTCs, which also point to the significant role the velocity distribution has in initiating the finger formation, while the modified Sherwood number scales the BTCs with respect to the inlet pressure. We summarize our findings as follows:

(1) In the homogeneous porous media, an initially nonuniform invasion due to a point source evolves into a uniform front, contrasting with the expected single-finger pattern in viscous fingering; however, increasing heterogeneity shifts this to a more pronounced, thinner single-finger pattern. This indicates that the invasion pattern is primarily dictated by the media's heterogeneity, with variations in viscosity further enhancing this pattern, underscoring the significant influence of the medium's inner structure on flow dynamics.

(2) In the homogeneous media, a uniform fluid invasion results in a consistent mixing front, while increased heterogeneity leads to less uniform, fingerlike patterns with the displacing fluid following a narrower path, leaving glycerol trapped on either side. This fingerlike invasion, initially guided by pore structure, evolves over time to favor paths of lower resistance and reduced viscosity, with mixing primarily occurring at the edges of the finger and affecting the overall fluid viscosity.

(3) The pore-scale heterogeneity in porous media affects both the viscosity and resistance within the flow cell, influencing the time taken for the invading fluid to achieve complete saturation and altering the rate of discharge. This discharge pattern, which follows the heterogeneity and inlet pressure, offers a macroscale Darcy measurement indicative of the underlying pore-scale processes and links changes in local velocity and viscosity with observable changes in fluid flow and invasion patterns at the macroscale.

Both heterogeneity and inlet pressure significantly influence the velocity distribution for miscible phase flow in porous media, affecting the displacement and mixing patterns of the invading fluid phase, as indicated by the BTC analysis. The BTC analysis reveals that higher inlet pressures enhance the velocity distribution, leading to distinct displacement patterns across varying heterogeneity levels, with more pronounced differences in velocity and mixing patterns observed at higher heterogeneity and pressure levels.

(4) The marked transition from a uniform front to finger formation in miscible fluid invasion and mixing patterns within porous media is governed by the velocity distribution, which is influenced by pore structure and pressure differences. This pattern change is captured by a modified Sherwood number, incorporating factors such as the convective mass transfer rate, diffusion rate, pore structure variance, and viscosity contrast, effectively linking these physical properties to the observed transition between uniform and fingered flow patterns in a phenomenological manner, and scaling the role of inlet pressure for the BTCs.

While our findings on the displacement and mixing mechanisms of miscible phase flow are limited to a small porous structure, they may still prove valuable for improving the invasion initiation in existing models of miscible multiphase flow, which are particularly important for geological and industrial processes. By demonstrating how fingering patterns and mixing behaviors in miscible phases are influenced by the heterogeneous structure and driving pressure, the research provides insights for refining predictive models used in applications such as geological carbon sequestration and hydrogen storage. It highlights the importance of considering both viscosity differences and pore-scale heterogeneity, which are missing in 2D Hele-Shaw cell models. The study also points to the limitations of 2D simulations in capturing the additional boundary effect on shear stress, which will be the subject of a future study. These insights are particularly relevant for environmental applications, such as the sequestration of supercritical CO_2 and its interaction with resident brine, as it ties the pore-scale displacement and mixing with the Darcy-scale observations measured for environmental and industrial processes.

ACKNOWLEDGMENTS

We thank Prof. Marco Dentz for his insightful comments and discussions, and Tongzhou Gan for performing additional experiments. Y.E. and Y.E.Y. acknowledge the support of the Israel Science Foundation (ISF Grant No. 801/20).

APPENDIX

In the Appendix, we present the raw images taken by the confocal microscope portraying the mixing and displacement of the high viscosity phase by the low viscosity phase (Fig. 6), and the BTC's are divided into levels of heterogeneity where for each heterogeneity level, we present all the applied inlet pressure before and after (part A and B in Fig. 7, respectively) scaling with the modified Sherwood number (Sh_{eff}). Multiplying the BTC's by the Sh_{eff} allows the curves to overlap with each other.

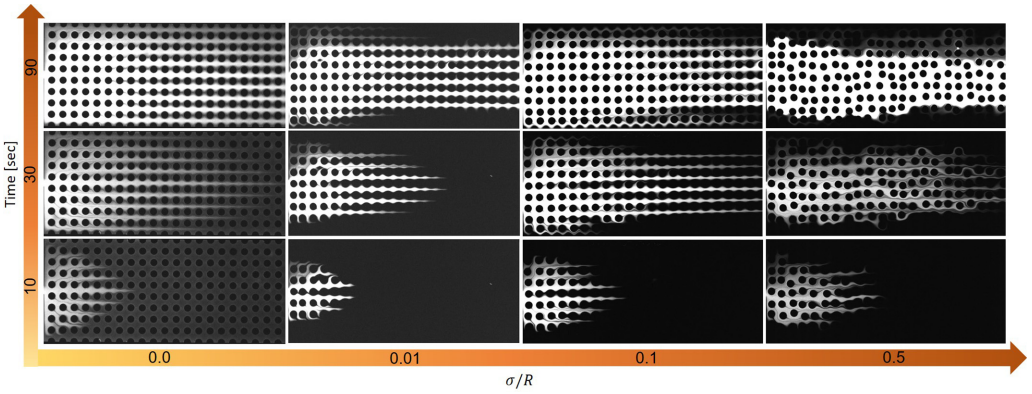

FIG. 6. Raw data of displacement and mixing pattern variation under a given inlet pressure of 30 mbar at 10, 30, and 90 s at heterogeneity levels of 0.0, 0.01, 0.1, and 0.5.

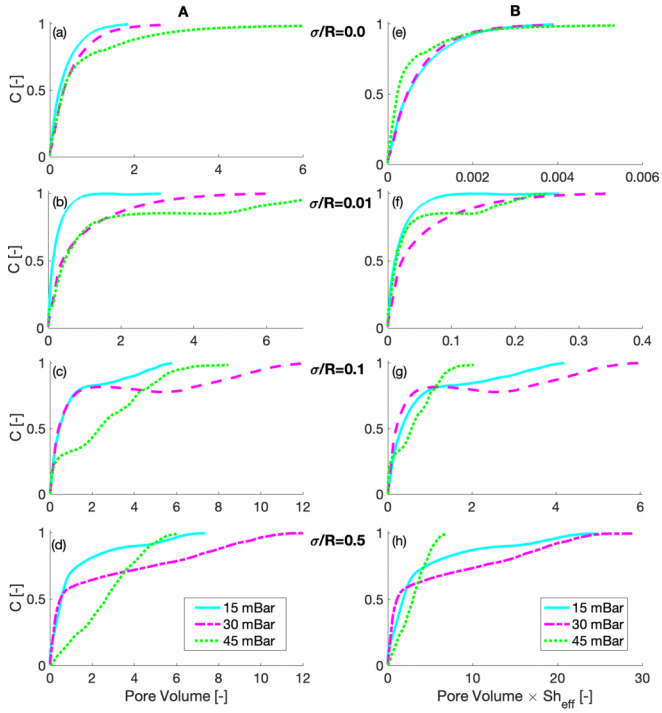

FIG. 7. A comparison of BTCs with a varying inlet pressure of 15, 30, and 45 mbar (dotted, dashed, and solid, respectively), A, before, and B, after multiplication of the PV with the modified Sherwood number (4), for heterogeneity's of $\sigma/R = 0.0$, 0.01, 0.1, and 0.5 [(a)–(d), and (e)–(h)], respectively).

[1] P. Barlow and E. Reichard, Saltwater intrusion in coastal regions of North America, Hydrogeol. J. **18**, 247 (2010).
[2] N. Heinemann, J. Alcalde, J. M. Miocic, S. J. Hangx, J. Kallmeyer, C. Ostertag-Henning, A. Hassanpouryouzband, E. M. Thaysen, G. J. Strobel, C. Schmidt-Hattenberger, Enabling large-scale hydrogen storage in porous media–the scientific challenges, Energy Environ. Sci. **14**, 853 (2021).
[3] S. Krevor, H. De Coninck, S. E. Gasda, N. S. Ghaleigh, V. de Gooyert, H. Hajibeygi, R. Juanes, J. Neufeld, J. J. Roberts, and F. Swennenhuis, Subsurface carbon dioxide and hydrogen storage for a sustainable energy future, Nat. Rev. Earth Environ. **4**, 102 (2023).
[4] R. J. Glass, J.-Y. Parlange, and T. S. Steenhuis, Wetting front instability: 1. Theoretical discussion and dimensional analysis, Water Resour. Res. **25**, 1187 (1989).
[5] B. Pan, X. Yin, Y. Ju, and S. Iglauer, Underground hydrogen storage: Influencing parameters and future outlook, Adv. Colloid Interface Sci. **294**, 102473 (2021).
[6] C. Tan and G. Homsy, Stability of miscible displacements in porous media: Rectilinear flow, Phys. Fluids **29**, 3549 (1986).
[7] R. Moosavi, A. Kumar, A. De Wit, and M. Schröter, Influence of mineralization and injection flow rate on flow patterns in three-dimensional porous media, Phys. Chem. Chem. Phys. **21**, 14605 (2019).
[8] M. A. Celia, J. M. Nordbotten, S. Bachu, M. Dobossy, and B. Court, Risk of leakage versus depth of injection in geological storage, Energy Procedia **1**, 2573 (2009).
[9] H. Deng, B. R. Ellis, C. A. Peters, J. P. Fitts, D. Crandall, and G. S. Bromhal, Modifications of carbonate fracture hydrodynamic properties by CO_2-acidified brine flow, Energy Fuels **27**, 4221 (2013).
[10] Y. Edery, M. Stolar, G. Porta, and A. Guadagnini, Feedback mechanisms between precipitation and dissolution reactions across randomly heterogeneous conductivity fields, Hydrol. Earth Syst. Sci. **25**, 5905 (2021).
[11] E. Shavelzon and Y. Edery, Shannon entropy of transport self-organization due to dissolution/precipitation reaction at varying Peclet number in an initially homogeneous porous media, Hydrol. Earth Syst. Sci. Discuss. **28**, 1803 (2024).
[12] B. Ellis, C. Peters, J. Fitts, G. Bromhal, D. McIntyre, R. Warzinski, and E. Rosenbaum, Deterioration of a fractured carbonate caprock exposed to CO_2-acidified brine flow, Greenhouse Gases Sci. Technol. **1**, 248 (2011).
[13] R. G. Fagin and C. H. Stewart, Jr., A new approach to the two-dimensional multiphase reservoir simulator, Soc. Pet. Eng. J. **6**, 175 (1966).
[14] A. Birtles and M. Reeves, Computer modelling of regional groundwater systems in the confined-unconfined flow regime, J. Hydrol. **34**, 97 (1977).
[15] G. M. Homsy, Viscous fingering in porous media, Annu. Rev. Fluid Mech. **19**, 271 (1987).
[16] L. Paterson, Fingering with miscible fluids in a Hele Shaw cell, Phys. Fluids **28**, 26 (1985).
[17] P. King, The fractal nature of viscous fingering in porous media, J. Phys. A: Math. Gen. **20**, L529 (1987).
[18] J.-D. Chen, Radial viscous fingering patterns in Hele-Shaw cells, Exp. Fluids **5**, 363 (1987).
[19] M. Hopp-Hirschler, M. S. Shadloo, and U. Nieken, Viscous fingering phenomena in the early stage of polymer membrane formation, J. Fluid Mech. **864**, 97 (2019).
[20] R. Luo, Y. Chen, and S. Lee, Particle-induced viscous fingering: Review and outlook, Phys. Rev. Fluids **3**, 110502 (2018).
[21] D. Pritchard, The linear stability of double-diffusive miscible rectilinear displacements in a Hele-Shaw cell, Eur. J. Mech., B: Fluids **28**, 564 (2009).
[22] S. Pramanik, A. De Wit, and M. Mishra, Viscous fingering and deformation of a miscible circular blob in a rectilinear displacement in porous media, J. Fluid Mech. **782**, R2 (2015).
[23] S. Nand, V. Sharma, S. K. Das, S. S. Padhee, and M. Mishra, Effect of Hele–Shaw cell gap on radial viscous fingering, Sci. Rep. **12**, 18967 (2022).
[24] J.-C. Bacri, D. Salin, and R. Woumeni, Three-dimensional miscible viscous fingering in porous media, Phys. Rev. Lett. **67**, 2005 (1991).
[25] L. Paterson, Radial fingering in a Hele Shaw cell, J. Fluid Mech. **113**, 513 (1981).

[26] R. L. Slobod and R. A. Thomas, Effect of transverse diffusion on fingering in miscible-phase displacement, Soc. Pet. Eng. J. **3**, 9 (1963).
[27] C. Nicolaides, B. Jha, L. Cueto-Felgueroso, and R. Juanes, Impact of viscous fingering and permeability heterogeneity on fluid mixing in porous media, Water Resour. Res. **51**, 2634 (2015).
[28] H. S. Rabbani, D. Or, Y. Liu, C.-Y. Lai, N. B. Lu, S. S. Datta, H. A. Stone, and N. Shokri, Suppressing viscous fingering in structured porous media, Proc. Natl. Acad. Sci. USA **115**, 4833 (2018).
[29] B. Zhao, C. W. MacMinn, and R. Juanes, Wettability control on multiphase flow in patterned microfluidics, Proc. Natl. Acad. Sci. USA **113**, 10251 (2016).
[30] B. Levaché and D. Bartolo, Revisiting the Saffman-Taylor experiment: Imbibition patterns and liquid-entrainment transitions, Phys. Rev. Lett. **113**, 044501 (2014).
[31] B. Berkowitz, H. Scher, and S. Stephen, Correction to "Anomalous transport in laboratory-scale, heterogeneous porous media", Water Resour. Res. **36**, 1371 (2000).
[32] A. Dagan and Y. Edery, Bifurcating paths: The relation between preferential pathways, channel splitting, under sampled regions, and tortuosity on the darcy scale, Adv. Water Resour. **184**, 104622 (2024).
[33] S. S. Gopalakrishnan, J. Carballido-Landeira, A. De Wit, and B. Knaepen, Relative role of convective and diffusive mixing in the miscible Rayleigh-Taylor instability in porous media, Phys. Rev. Fluids **2**, 012501(R) (2017).
[34] B. Jha, L. Cueto-Felgueroso, and R. Juanes, Fluid mixing from viscous fingering, Phys. Rev. Lett. **106**, 194502 (2011).
[35] M. C. Kim and S. Pramanik, Miscible viscous fingering in a packed cylindrical column: Theory and numerics, Phys. Rev. Fluids **8**, 013901 (2023).
[36] Q. Yuan, B. Ling, and S. A. Aryana, New phase diagram of miscible viscous fingering instabilities in porous media with dead-end pores, Phys. Fluids **34**, 092109 (2022).
[37] T. Lei and K. H. Luo, Pore-scale simulation of miscible viscous fingering with dissolution reaction in porous media, Phys. Fluids **33**, 034134 (2021).
[38] S. Afshari, S. H. Hejazi, and A. Kantzas, Role of medium heterogeneity and viscosity contrast in miscible flow regimes and mixing zone growth: A computational pore-scale approach, Phys. Rev. Fluids **3**, 054501 (2018).
[39] M. Barzan and F. Hajiesmaeilbaigi, Investigation the concentration effect on the absorption and fluorescence properties of Rhodamine 6G dye, Optik **159**, 157 (2018).
[40] M. Sahimi, Flow phenomena in rocks: From continuum models to fractals, percolation, cellular automata, and simulated annealing, Rev. Mod. Phys. **65**, 1393 (1993).
[41] K. Alim, S. Parsa, D. A. Weitz, and M. P. Brenner, Local pore size correlations determine flow distributions in porous media, Phys. Rev. Lett. **119**, 144501 (2017).
[42] Z. Alhashmi, M. Blunt, and B. Bijeljic, The impact of pore structure heterogeneity, transport, and reaction conditions on fluid–fluid reaction rate studied on images of pore space, Transp. Porous Media **115**, 215 (2016).
[43] B. Bijeljic and M. J. Blunt, Pore-scale modeling and continuous time random walk analysis of dispersion in porous media, Water Resour. Res. **42**, 2005WR004578 (2006).
[44] B. Bijeljic, A. Raeini, P. Mostaghimi, and M. J. Blunt, Predictions of non-Fickian solute transport in different classes of porous media using direct simulation on pore-scale images, Phys. Rev. E **87**, 013011 (2013).
[45] Y. Edery, I. Dror, H. Scher, and B. Berkowitz, Anomalous reactive transport in porous media: Experiments and modeling, Phys. Rev. E **91**, 052130 (2015).
[46] S. Aramideh, P. P. Vlachos, and A. M. Ardekani, Pore-scale statistics of flow and transport through porous media, Phys. Rev. E **98**, 013104 (2018).
[47] P. K. Kang, P. De Anna, J. P. Nunes, B. Bijeljic, M. J. Blunt, and R. Juanes, Pore-scale intermittent velocity structure underpinning anomalous transport through 3-D porous media, Geophys. Res. Lett. **41**, 6184 (2014).
[48] B. Bijeljic, P. Mostaghimi, and M. J. Blunt, Signature of non-Fickian solute transport in complex heterogeneous porous media, Phys. Rev. Lett. **107**, 204502 (2011).

[49] Y. Edery, S. Geiger, and B. Berkowitz, Structural controls on anomalous transport in fractured porous rock, Water Resour. Res. **52**, 5634 (2016).

[50] Y. Nishijima and G. Oster, Diffusion in glycerol-water mixture, Bull. Chem. Soc. Jpn. **33**, 1649 (1960).

[51] J.-H. Kim, J. A. Ochoa, and S. Whitaker, Diffusion in anisotropic porous media, Transp. Porous Media **2**, 327 (1987).

[52] M. Quintard, Diffusion in isotropic and anisotropic porous systems: Three-dimensional calculations, Transp. Porous Media **11**, 187 (1993).

[53] M. Quintard and S. Whitaker, Transport in ordered and disordered porous media: Volume-averaged equations, closure problems, and comparison with experiment, Chem. Eng. Sci. **48**, 2537 (1993).

[54] S. Beyhaghi and K. Pillai, Estimation of tortuosity and effective diffusivity tensors using closure formulation in a sintered polymer wick during transport of a nondilute, multicomponent liquid mixture, Spec. Top. Rev. Porous Media: Int. J. **2**, 267 (2011).